Human Molecular Genetics, 2017, Vol. 26, No. 17 3362–3374

doi: 10.1093/hmg/ddx224
Advance Access Publication Date: 13 June 2017
Original Article

ORIGINAL ARTICLE

Comparison of spinocerebellar ataxia type 3 mouse models identifies early gain-of-function, cell-autonomous transcriptional changes in oligodendrocytes

Biswarathan Ramani[1], Bharat Panwar[2], Lauren R. Moore[1], Bo Wang[1,†], Rogerio Huang[1], Yuanfang Guan[2] and Henry L. Paulson[1,*]

[1]Department of Neurology and [2]Department of Computational Medicine and Bioinformatics, University of Michigan, Ann Arbor, MI, USA

*To whom correspondence should be addressed at: 109 Zina Pitcher Place, A. Alfred Taubman Biomedical Science Research Building, Ann Arbor, MI 48109-2200, USA. Tel: 734 6156156; Fax: 734 6155655; Email: henryp@med.umich.edu

Abstract

Spinocerebellar ataxia type 3 (SCA3) is a neurodegenerative disorder caused by a polyglutamine-encoding CAG repeat expansion in the *ATXN3* gene. This expansion leads to misfolding and aggregation of mutant ataxin-3 (ATXN3) and degeneration of select brain regions. A key unanswered question in SCA3 and other polyglutamine diseases is the extent to which neurodegeneration is mediated through gain-of-function versus loss-of-function. To address this question in SCA3, we performed transcriptional profiling on the brainstem, a highly vulnerable brain region in SCA3, in a series of mouse models with varying degrees of ATXN3 expression and aggregation. We include two SCA3 knock-in mouse models: our previously published model that erroneously harbors a tandem duplicate of the CAG repeat-containing exon, and a corrected model, introduced here. Both models exhibit dose-dependent neuronal accumulation and aggregation of mutant ATXN3, but do not exhibit a behavioral phenotype. We identified a molecular signature that correlates with ATXN3 neuronal aggregation yet is primarily linked to oligodendrocytes, highlighting early white matter dysfunction in SCA3. Two robustly elevated oligodendrocyte transcripts, *Acy3* and *Tnfrsf13c*, were confirmed as elevated at the protein level in SCA3 human disease brainstem. To determine if mutant ATXN3 acts on oligodendrocytes cell-autonomously, we manipulated the repeat expansion in the variant SCA3 knock-in mouse by cell-type specific Cre/LoxP recombination. Changes in oligodendrocyte transcripts are driven cell-autonomously and occur independent of neuronal ATXN3 aggregation. Our findings support a primary toxic gain of function mechanism and highlight a previously unrecognized role for oligodendrocyte dysfunction in SCA3 disease pathogenesis.

Introduction

Spinocerebellar ataxia type 3 (SCA3), the most common dominantly inherited ataxia, is a fatal disease characterized by progressive motor deficits and preferential degeneration of the brainstem, cerebellum and spinal cord (1). SCA3 is caused by a polyglutamine-encoding CAG repeat expansion in the *ATXN3* gene, placing it among the polyglutamine diseases which also include five other SCAs (SCA1, 2, 6, 7, and 17), Huntington disease, spinobulbar muscular atrophy and dentatorubralpallidoluysian atrophy. SCA3 and other polyglutamine diseases are typified by the presence of ubiquitin-positive neuronal inclusions containing the disease protein (2). While inclusions may not be toxic (3–5), numerous studies point to protein misfolding

†Present address: Department of Dermatology, Ruijin Hospital, School of Medicine, Shanghai Jiaotong University, Shanghai, China.
Received: April 7, 2017. **Revised:** May 5, 2017. **Accepted:** May 31, 2017

and aggregation of the disease protein in neurons as a central driver of disease pathogenesis through gain-of-function mechanisms (6–8).

Although more than two decades have passed since the disease-causing mutation was identified, several key issues remain unresolved in SCA3. First, early molecular changes in the SCA3 brain have not been explored systematically, particularly with respect to the highly vulnerable brainstem. Second, the extent to which molecular changes are driven by a dominant gain-of-function mechanism related to ATXN3 misfolding or aggregation remains poorly defined. Third, the potential contribution to disease of a loss-of-function in ATXN3, a deubiquitinating enzyme implicated in protein quality control, remains contested (9–12). And finally, whereas ATXN3 aggregates primarily accumulate in neurons, the extent to which ATXN3 is expressed in nonneuronal cells such as glia and the possible disease consequences have rarely been investigated (13).

To begin addressing these various questions, we sought to identify early transcriptional changes in multiple mouse models of SCA3 that differ with respect to ATXN3 expression and aggregation. Existing SCA3 mouse models have employed transgenic or viral overexpression of the human *ATXN3* cDNA (14), transgenic expression of the full *ATXN3* disease gene from a yeast artificial chromosome (YAC) (15), or 'knock-in' of a pathogenic CAG expansion into the endogenous *Atxn3* gene (16,17). Knock-in mouse models are particularly useful for studying early molecular changes and potential loss-of-function, since expression of the mutant gene under the endogenous promoter most closely mimics the physiological levels and expression pattern of ATXN3 in humans. Our access to two distinct SCA3 knock-in mouse models, YAC transgenic mice expressing the full human *ATXN3* gene with normal or expanded repeat, and *Atxn3* knockout mice enabled us to investigate the extent to which transcriptional changes are associated with ATXN3 aggregation versus ATXN3 levels. Because the majority of aggregation-associated transcripts mapped to oligodendrocytes, we further assessed whether transcriptional changes in oligodendrocytes occur cell-autonomously.

Results

Generation of a corrected SCA3 knock-in mouse and comparison of its effects on ATXN3 expression and aggregation

The current study takes advantage of our recently generated SCA3 knock-in mouse model, among other models. We previously reported this SCA3 knock-in mouse harboring a CAG repeat expansion of 82 repeats in exon 10 of the endogenous *Atxn3* locus (16). These mice exhibit marked ATXN3 aggregation and low levels of soluble mutant ATXN3. They also express a truncated *Atxn3* transcript missing the final coding 11th exon, encoding a previously identified ATXN3 isoform that is known to be aggregate-prone (18). In subsequently sequencing the *Atxn3* gene from exons 9 to 11 to identify possible cis-acting modifiers of *Atxn3* splicing, we discovered that the reported SCA3 knock-in mouse erroneously harbored a tandem copy of the original targeting vector used for homologous recombination, resulting in two copies of mutant exon 10 separated by an intron 9/intron10 hybrid region (Fig. 1A). We now designate this original knock-in mouse the 'dupKi' line and, simultaneously with this report, submitted a corrigendum to our previous publication that will be published.

The presence of two remaining FRT sequences in dupKi mice allowed us to perform a second round of recombination to generate the corrected SCA3 knock-in mouse line, designated the 'Ki' line (Fig. 1A). Supplementary Material, Figure S1 provides a more detailed genetic map of the two SCA3 knock-in lines, along with PCR and genome sequencing evidence-confirming correction of the duplication (Supplementary Material, Fig. S1). The dupKi line also harbors two LoxP sequences adjacent to the FRT sequences that we utilize later in this study to explore cell-type specific transcriptional alterations. A PGK promoter-driven thymidine kinase gene is also retained in the dupKi line between the two mutant exon 10s. As described further in this manuscript, the presence of the thymidine kinase gene may accelerate the mis-splicing that generates the truncated *Atxn3* transcript missing exon 11.

We compared disease features in these two otherwise genetically identical SCA3 knock-in mouse lines. We first examined ATXN3 expression and aggregation in the brains of heterozygous (het) mice of both lines. Ki-het and dupKi-het mice both showed increased levels of high molecular weight (HMW) ATXN3 species (Fig. 1B) resolved on polyacrylamide gradient gels, although the levels of HMW ATXN3 were markedly higher in dupKi-het mice. Conversely, Ki-het mice show higher levels of soluble, monomeric mutant ATXN3. Mice that are homozygous for the corrected allele (Ki-hom mice) continue to express a high level of soluble, monomeric mutant ATXN3 in the absence of wild-type (nonexpanded) ATXN3 (Supplementary Material, Figure S1).

To further characterize differences in ATXN3 aggregation in the two SCA3 knock-in lines, we performed ATXN3 immunohistochemical staining on one-year-old Ki and dupKi brains. As described before (16), dupKi-het mice show robust intranuclear ATXN3 accumulation, both diffuse and punctate, as well as larger intraneuronal inclusions throughout the brain (Fig. 1C). The dupKi-het mice also exhibit large extranuclear aggregates in neurons, particularly in the stratum radiatum of the hippocampus. In contrast, Ki-het mice show no noticeable aggregate pathology and ATXN3 immunohistochemistry is indistinguishable from that of wild-type mice. Homozygous Ki mice (Ki-hom), however, exhibit intranuclear concentration of ATXN3 in brainstem neurons, and with aging, large neuropil aggregates accumulate in the stratum radiatum, reminiscent of the aggregates in dupKi mice.

To characterize possible physical and behavioral abnormalities in the corrected Ki line, we assessed weight and motor performance in 53-60 week old mice. On average, dupKi-het mice tend to be slightly smaller than wild-type or Ki-het mice, but both knock-in lines otherwise appear healthy. Neither Ki-het nor dupKi-het mice show deficits on motor behavior tasks including balance beam, rotarod, and open field exploration (Supplementary Material, Fig. S2).

To explore factors underlying the marked differences in aggregation between Ki and dupKi mice, we explored *Atxn3* splicing in both lines. This also allowed us to determine if the CAG expansion in exon 10 drives *Atxn3* mis-splicing in the brain (16,19). We previously showed that dupKi mice have impaired splicing of exon 10/exon 11, generating an intron 10-containing *Atxn3* transcript (*Atxn3*-10e) that lacks the final exon 11. In contrast, by RT-PCR the corrected Ki line does not exhibit enhanced *Atxn3* mis-splicing and instead generates the full-length mutant *Atxn3* transcript (*Atxn*-11e) (Fig. 2A). These results suggest that *Atxn3* mis-splicing downstream of exon 10 is not promoted by the expanded CAG repeat but, rather, may be an artifact of the presence of a PGK-driven TK gene after the first mutant exon 10.

We further assessed whether the tandem copies of mutant exon 10 in dupKi mice could splice together to generate a

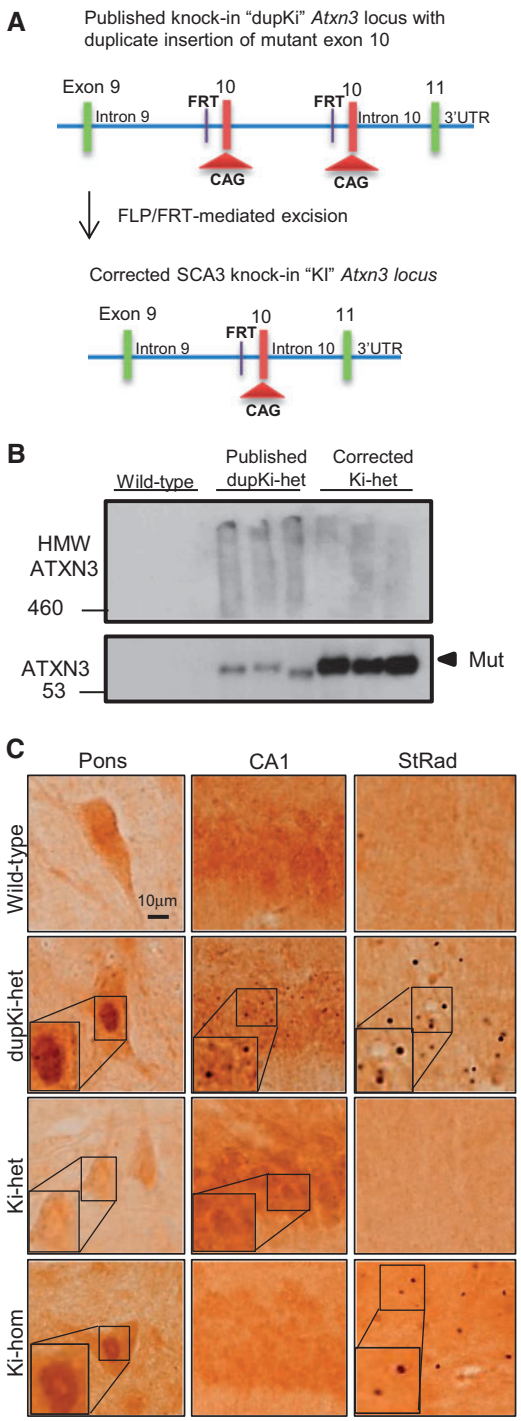

Figure 1. Comparison of an atypical SCA3 knock-in mouse model and a corrected knock-in line reveals distinct differences in ataxin-3 (ATXN3) expression and aggregation in the brain. (**A**) Simplified schematic of the insertion in our previously reported knock-in mice which harbor a duplicate tandem insertion of the targeting vector containing the CAG repeat-expansion in exon 10 (dupKi). FLP-FRT recombination allowed us to excise the duplication and generate a corrected SCA3 knock-in mouse line (Ki). (**B**) By Western blot, brain lysates of one-year-old heterozygous dupKi (dupKi-het) mice exhibit increased high molecular weight (HMW) aggregated ATXN3 and reduced mutant (mut) ATXN3 monomer (arrowhead), compared to corrected Ki-het mice. (**C**) Anti-ATXN3 immunohistochemistry demonstrates robust ATXN3 accumulation and puncta in brain regions of 1-year-old dupKi-het mice, including the pons and hippocampus (CA1 and stratum radiatum (StRad)), whereas Ki-het mice show no noticeable ATXN3 accumulation. Homozygous Ki mice (Ki-hom) exhibit modest ATXN3 accumulation in brainstem neuronal nuclei, along with large neuropil inclusions in the StRad, similar to heterozygous dupKi mice.

double-exon 10 *Atxn3* transcript. Using 5' RACE and PCR on brain-derived RNA of homozygous dupKi and Ki mice, we amplified a band consistent with this transcript in dupKi mice (Fig. 2B) although we were unable to capture enough products for sequencing. Nonetheless, these findings indicate that the Ki mouse line predominantly expresses the full-length mutant ATXN3 encoded from *Atxn3-11e*, whereas the dupKi line expresses a truncated mutant ATXN3 encoded from *Atxn3-10e* and possibly an artifactual ATXN3 'isoform' containing duplicate exon 10s (Fig. 2B). In this double exon 10 isoform, the second exon 10 is predicted to be out of frame with the first exon 10, resulting in a polyQ tract followed by an equal-sized polyserine tract, in turn followed by two arginines and a stop codon (Fig. 2C). We could not identify a soluble monomeric band corresponding to this ATXN3 species, likely reflecting its high aggregation propensity.

To determine the relative abundance of the different transcripts in the dupKi mice, we examined the levels of *Atxn3* transcripts in dupKi mice from RNA-seq analysis (Supplementary Material, Fig. S3). This showed that dupKi-het mice express full-length (3'UTR-containing) *Atxn3* transcript at similar levels to wild-type mice; of note, the full-length *Atxn3* transcript of dupKi mice should not form without including both mutant exon 10s and therefore must be the double-exon 10 *Atxn3* transcript. In contrast, dupKi-het mice express ~3-fold higher levels of mutant *Atxn3* transcripts containing exons 1 through 9; and the majority of this signal in dupKi-het mice derives from mutant *Atxn3*-10e transcript, which we also observed previously (16). In short, the dupKi-het mice express wild-type full-length *Atxn3*, mutant *Atxn3*-10e and double-exon 10 mutant *Atxn3* transcripts at approximately 1:~3:1 relative levels (Supplementary Material, Fig. S3). Interestingly, this result suggests the 3'UTR contains a feedback mechanism to maintain homeostatic levels of full-length *Atxn3* transcript, as impaired splicing to the 3'UTR in dupKi mice may drive upregulation of *Atxn3* transcripts upstream of exon 10. The corrected Ki shows no differences in *Atxn3* transcript levels compared to wild-type (not shown).

In summary, the corrected Ki mouse line no longer exhibits accelerated mis-splicing, expresses high soluble levels of mutant full length ATXN3, and exhibits dose-dependent ATXN3 aggregation and accumulation in the brain, albeit less than dupKi-het mice. The existence of both the Ki and dupKi lines extends the range of available mouse models for molecular studies of SCA3. In this manuscript, we exploit the differences in ATXN3 expression and aggregate pathology in a range of mouse lines, including both Ki lines, to identify molecular correlates to mutant ATXN3 expression or aggregation.

Disease gene expression is associated with early transcriptional changes in the pons

Transcriptional profiling has uncovered transcriptional dysregulation as a frequent feature of polyQ diseases (20–23). To explore such dysregulation associated with ATXN3 expression or aggregation, we employed RNA-sequencing (RNA-seq) to investigate a series of mouse models differing in the degree of ATXN3 expression or aggregation. Table 1 lists the eight genotypes used for RNA-seq studies, as well as the number of ATXN3-encoding genes and relative aggregate burden in the brain for each mouse line. The tested mouse genotypes include wild-type mice, heterozygous and homozygous Ki and dupKi mice, YAC transgenic mice overexpressing the full-length human *ATXN3* gene with or without an expanded repeat (YAC84Q and

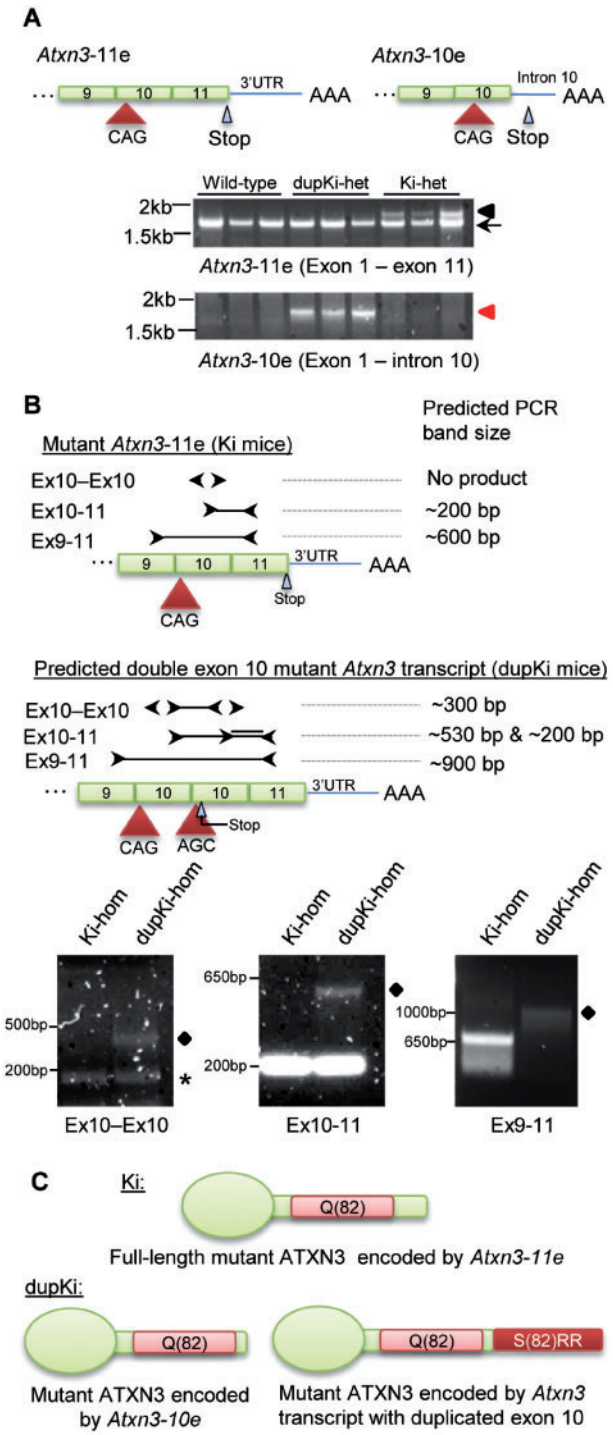

Figure 2. Ki mice do not exhibit *Atxn3* mis-splicing, whereas dupKi mice express different aberrantly-generated *Atxn3* transcripts. (**A**) We examined *Atxn3* transcripts with alternative splicing of exon 11, including a shorter 10-exon containing *Atxn3* transcript (*Atxn3*-10e) and a full-length transcript containing all 11 exons (*Atxn3*-11e), both diagrammed at the 3' end. RT-PCR demonstrates that Ki mice express wild-type (arrow) and mutant (arrowhead) *Atxn3*-11e transcript, whereas dupKi-het mice do not express detectable mutant *Atxn3-11e* transcript. Instead, dupKi-het mice express the previously described *Atxn3-10e* transcript (red arrowhead) (16), which is not elevated in Ki mice. (**B**) To test for a predicted *Atxn3* transcript containing both mutant exon 10s spliced together in dupKi mice, we performed different PCR reactions on *Atxn3* cDNA that was reverse-transcribed with a primer against the *Atxn3* 3'UTR in homozygous Ki and dupKi mice brain RNA. We provide a diagram of the PCR primers and predicted sizes of amplification products for exon 9 to 11, exon 10 to 11, and exon 10 to exon 10 (3' to 5' ends) in Ki and dupKi mice. All three PCR reactions revealed signals in a dupKi-hom mouse consistent with the predicted size for a duplicated exon 10 *Atxn3* transcript (diamond). *Non-specific band. (**C**) Diagram of predicted mutant ATXN3 isoforms in the different SCA3 knock-in lines. Ki mice predominantly express the full-length mutant ATXN3 isoform encoded by the *Atxn3-11e* transcript. In contrast, dupKi mice predominantly express a mutant ATXN3 isoform slightly truncated at the carboxy-terminus, encoded by the *Atxn3-10e* transcript, and likely express a predicted mutant ATXN3 encoded from a duplicated exon 10-containing *Atxn3* transcript, in which the expanded repeat in the second exon 10 encodes expanded polyserine followed by two arginines and a stop.

Table 1. The mouse models utilized for RNA sequencing studies exhibit a range of ATXN3 expression level and aggregation in the brain. The number of ATXN3-encoding genes is designated by a plus sign (+) for each gene that expresses ATXN3 endogenously or transgenically, and a minus sign (-) if no ATXN3 is expressed as in ATXN3 knockout mice (ATXN3-KO). The relative amount of ATXN3 aggregation in the brain, based on IHC and Western blotting data, is indicated by the number of + signs, and a - if ATXN3 aggregation is not detected

Mouse genotype	# of ATXN3-encoding genes	ATXN3 aggregation
Wild-type	++	–
YAC84Q	++ ++	++ ++
YAC15Q	++ ++ ++	–
Ki-het	++	+
Ki-hom	++	++
dupKi-het	++	+++
dupKi-hom	++	++ ++
ATXN3-KO	–	–

YAC15Q), and *Atxn3* knockout mice (ATXN3-KO). The two Ki lines are described above. The YAC84Q mice display robust ATXN3 accumulation and aggregation throughout the brain (15). The YAC15Q transgenic mouse harbors four copies of the *ATXN3* gene with a normal sized CAG repeat of 15, and thus overexpresses non-expanded ATXN3 but does not show any signs of aggregation (15). Finally, we included *Atxn3*-KO mice in our study to assess potential loss-of-function changes in SCA3, an important unanswered question in the field (24).

We performed two separate RNA-seq runs on 22 to 24-week-old pontine tissue, a brainstem region known to be heavily affected in human SCA3. The first run included wild-type ($n=6$), hemizygous YAC84Q ($n=4$), hemizygous YAC15Q ($n=4$), Ki-het ($n=4$), Ki-hom ($n=4$), and dupKi-het ($n=6$) mice. We performed a second run with wild-type ($n=3$), ATXN3-KO ($n=3$), and dupKi-hom ($n=3$) mice to identify potential correlations between transcriptional changes and loss of ATXN3 function. RNA reads were aligned and differential expression was calculated by both DESeq and CuffDiffs software. We first employed DESeq to generate lists of differentially expressed (DE) transcripts relative to wild-type, using a threshold of adjusted *P*-value of less than 0.1 and fold-change <0.8 or >1.2. We favored using *P*-value of 0.1 rather than 0.05 to allow for a more inclusive list of DE transcripts to help us maximize overlapping changes across different genotypes. We then generated FPKM values through CuffDiffs for all transcripts to visualize gene expression for individual mice in a heat map format.

We tabulated DE transcripts for each genotype to assess whether differences in ATXN3 expression or aggregation correlated with the degree of transcriptional perturbation (Fig. 3A). Remarkably, overexpression of non-expanded ATXN3 elicited few transcriptional changes (only 26 DE transcripts in YAC15Q

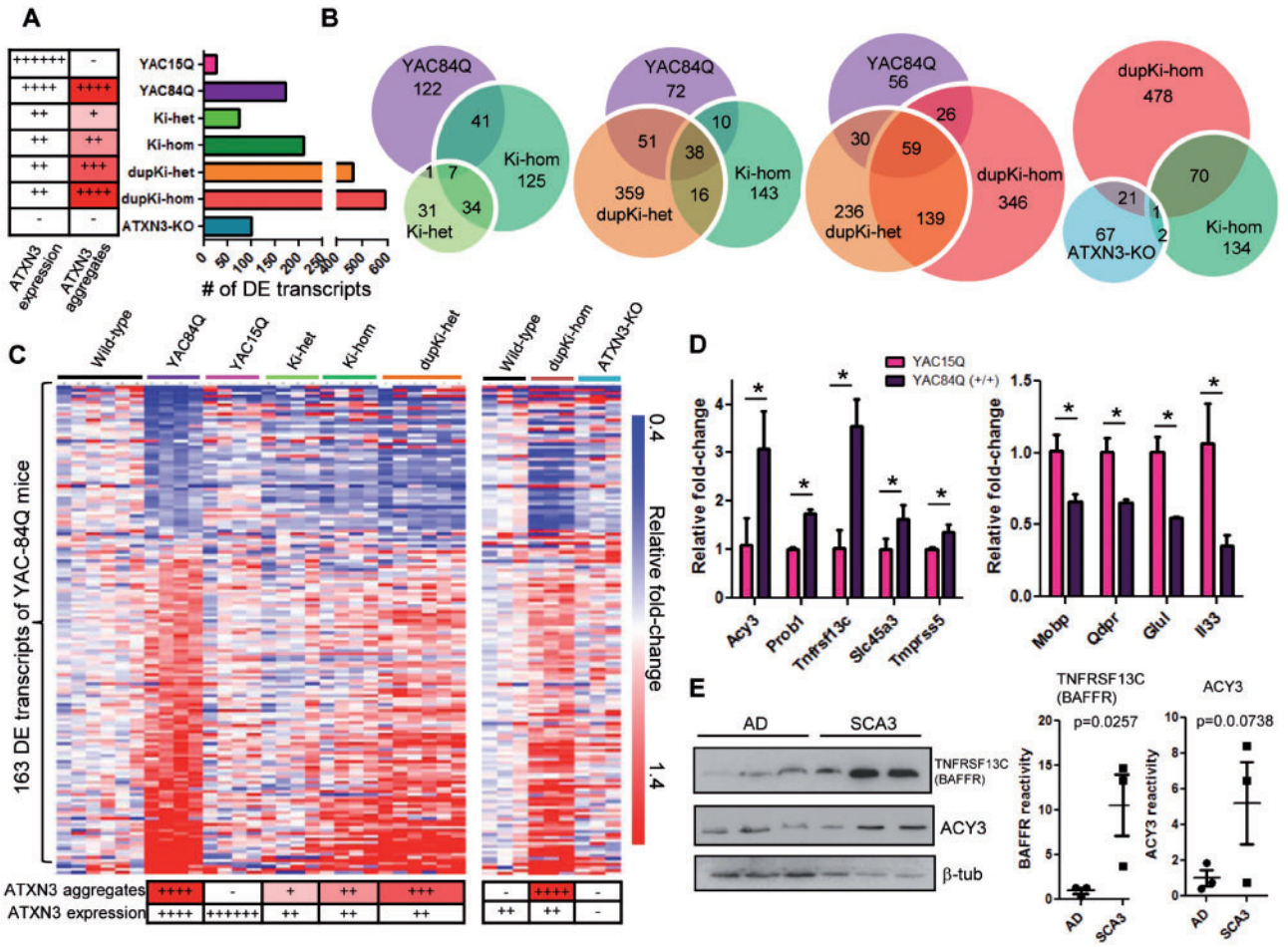

Figure 3. RNA-seq of the pons in mouse lines differing in ATXN3 expression and aggregation identifies transcriptional correlates to ATXN3 aggregation that are also altered in SCA3 human brainstem. (**A**) Total number of differentially expressed (DE) transcripts in the different mouse models correlates with the level of ATXN3 aggregation in a gene dose-dependent manner. Left, a table demonstrating ATXN3 expression level and ATXN3 aggregation for each genotype, with aggregation color-coded by red intensity corresponding to the amount of ATXN3 aggregation in each genotype. (**B**) Venn diagrams of the overlap in DE transcripts across mouse lines show a greater degree of shared transcripts between mice with higher ATXN3 aggregation, with the greatest overlap occurring between dupKi and YAC84Q mice, both of which have robust aggregation. In contrast, ATXN3-KO mice shared relatively few DE transcripts with any SCA3 mouse model, including Ki-hom and dupKi-hom mice, which do not express any wild-type ATXN3. (**C**) Visualization of the relative fold-change for 163 DE transcripts of YAC84Q mice as a heat map shows a concordant transcriptional signature in genotypes exhibiting increased ATXN3 aggregation. ATXN3-KO and dupKi-hom mice were profiled in an independent experiment and are shown separately. (**D**) Quantitative RT-PCR (qRT-PCR) confirmed key upregulated and downregulated candidate genes in the pons of homozygous YAC84Q mouse ($n = 3$) relative to YAC15Q mice ($n = 3$). *$P < 0.05$ by Student's *t*-test. (**E**), Left, Western blot showing increased TNFRSF13C and ACY3 signal in SCA3 human brainstem lysates compared to Alzheimer disease brainstem controls (AD). Right, graphs plotting the relative signal intensity from the blots on the left, with Student's *t*-test *P*-values shown above.

mice relative to wild-type mice), whereas YAC84Q mice, despite having fewer copies of the ATXN3 transgene, had 171 DE transcripts. Ki-het and Ki-hom mice had 73 and 208 DE transcripts respectively, suggesting a dose-dependent relationship between mutant ATXN3 expression and transcriptional dysregulation. The dupKi-het and dupKi-hom mice showed the most changes, 464 and 595 DE transcripts respectively, indicating prominent transcriptional perturbation in these lines with robust ATXN3 aggregation. ATXN3-KO mice showed moderate transcriptional changes, with 100 DE transcripts. Overall, the degree of mutant ATXN3 aggregation in a given line directly correlated with greater transcriptional dysregulation in a dose-dependent manner.

Venn diagrams mapping the overlap of DE transcripts across different genotypes revealed that the highest number of DE transcripts is shared between mouse lines displaying increased ATXN3 aggregation (Fig. 3B). For example, whereas only 8 DE transcripts are shared between YAC84Q and Ki-het mice, an additional 41 transcripts are shared between YAC84Q and Ki-hom mice, and the aggregate-rich dupKi-het and YAC84Q mice share 89 transcripts, the greatest overlap between two separate mouse models. Finally, whereas dupKi-hom and Ki-hom mice share 71 DE transcripts, they share far fewer DE transcripts with ATXN3-KO mice (only 22 and 3, respectively), implying that the basis of transcriptional alterations in mutant ATXN3 expressing lines is not due to a loss of ATXN3 function.

We generated heat maps to gauge the extent to which the DE transcripts identified in YAC84Q mice were shared across the various genotypes (Fig. 3C). This heat map revealed a transcriptional signature in the pons that correlates with the degree of ATXN3 aggregation but not ATXN3 levels. The vast majority of DE transcripts of YAC84Q mice changed concordantly in dupKi-het mice, suggesting that many transcripts beyond the 41 identified shared DE transcripts trend together in dupKi-het and YAC84Q mice. The heat map also suggests that early transcriptional changes in disease tend to be downregulated

transcripts (for example, those that occur with low levels of mutant ATXN3 aggregation in Ki-het mice). As aggregation level increases from Ki-hom to dupKi-het to dupKi-hom mice, the number of upregulated transcripts increases, as do the strength of transcriptional changes.

To ensure reproducibility and to identify transcripts that might serve as biomarkers correlating with disease protein aggregation, we verified by quantitative RT-PCR (qRT-PCR) a panel of the most upregulated and downregulated DE transcripts in the pons of YAC84Q mice. In ~40-week-old homozygous YAC84Q mice, we confirmed selective upregulation of *Acy3, Prob1, Tnfrsf13c, Slc45a3*, and *Tmprss5*, and selective downregulation of *Mobp, Qdpr, Glul*, and *Il33* compared to age-matched YAC-15Q mice (Fig. 3D) in the pons. Two DE transcripts, *Polr2a* and *Smoc1*, were not confirmed as significantly altered (not shown).

Of these tested transcripts, *Acy3* and *Tnfrsf13c* were among the most consistently and robustly upregulated. Although they are upregulated in Ki-hom, dupKi-het, and dup-Ki hom mice, they are not significantly altered in Ki-het mice, suggesting that the changes correlate with ATXN3 aggregation in a dose-dependent manner. We also examined these candidates at the protein level and found that TNFRSF13C and ACY3 protein levels were elevated in two of three SCA3 human brainstem samples compared to Alzheimer disease (AD) brainstem controls (Fig. 3E). These results provide confidence that our comparative studies on SCA3 mouse models have some predictive value for the human disease.

Altered transcripts in the pons of SCA3 mouse models are associated with oligodendrocyte pathways

We performed bioinformatics analyses of the DE transcripts across different genotypes in an effort to pinpoint the basis of transcriptional changes. We first focused on the 38 DE transcripts shared between three distinct aggregate-prone mouse models: YAC84Q, Ki-hom, and dupKi-het mice (Fig. 4A and Supplementary Material, Table S1). By gene enrichment analysis (25), five of the 38 genes (*Pmp22*, *Klk6*, *Mal*, *Tspan2*, and *Aspa*) belong to gene ontology categories related to myelination and myelin formation (Fig. 4A), pointing to possible alterations in oligodendrocytes. Consistent with this finding, Ingenuity® Pathway Analysis of all DE transcripts in YAC15Q, Ki-het, Ki-hom, dupKi-het, and YAC84Q mice highlighted categories related to demyelination, but again only in mice displaying significant ATXN3 aggregation (Fig. 4B and Supplementary Material, Fig. S4).

The finding that numerous DE transcripts are related to demyelination categories prompted us to examine whether many of the 38 DE transcripts shared across aggregate-prone lines associate with oligodendrocytes. Using the Brain-SEQ public database, which reports the expression level of each transcript across different cell types of the nervous system (26), we were able to bin 34 of the 38 transcripts into a cell type of highest expression. The vast majority of these transcripts are expressed at the highest level in oligodendrocytes, particularly myelinating oligodendrocytes (Fig. 4C). While ATXN3 aggregates are believed to accumulate primarily in neurons, Brain-SEQ demonstrated that *Atxn3* is expressed in cells throughout the nervous system, including in oligodendrocytes (Fig. 4D). Indeed, co-immunofluorescent staining for ATXN3 and OLIG2, which stains oligodendrocyte nuclei, showed ATXN3 signal in oligodendrocytes of homozygous YACQ84Q mice (Fig. 4E) which is clearly increased from wild-type oligodendrocytes. These findings raise the question of whether oligodendrocytes undergo transcriptional perturbations due to mutant ATXN3 expression, and if so, whether it occurs via cell-autonomous or non-cell-autonomous effects.

Oligodendrocyte-specific deletion of an expanded CAG repeat rescues oligodendrocyte-associated transcriptional changes

The above results reveal transcriptional changes associated with oligodendrocytes, particularly in mouse models showing robust aggregation. And yet the aggregation in these models appears to primarily reside in neurons, not oligodendrocytes. To assess whether the contribution of aggregation-prone ATXN3 to alterations of oligodendrocyte transcripts occurs in a cell-autonomous manner, we exploited the presence of two LoxP sequences in the dupKi line to excise the exon 10 duplication in a cell-type-specific manner (Fig. 5A). We crossed dupKi mice to mice expressing Cre recombinase either under a Nestin promoter (dupKi-het + N-Cre) to correct the duplication throughout many cell-types of the brain (including neurons and oligodendrocytes), or under an Olig2 promoter (dupKi-het + O-Cre) to correct the duplication only in oligodendrocytes. We examined dupKi-het + N-Cre and dupKi-het + O-Cre mice independently, comparing each mouse with their respective wild-type or dupKi-het littermates, to determine if correction of the duplication rescues *Atxn3* mis-splicing, ATXN3 aggregation, and oligodendrocyte-associated transcriptional changes.

As shown in Figure 5B, Nestin-Cre expression in dupKi mice restores normal *Atxn3* splicing in the brain: RT-PCR of pontine RNA showed reduced *Atxn3*-10e signal and increased *Atxn3*-11e signal in dupKi-het + N-Cre mice, similar to that of the Ki line. In contrast, Cre expression only in oligodendrocytes failed to change *Atxn3*-10e or *Atxn3*-11e levels in dupKi-mice (Fig. 5C and D). qRT-PCR confirmed that *Atxn3*-10e is significantly reduced in dupKi-het + N-Cre mice but not in dupKi + O-Cre mice (Fig. 5D). Thus, the majority of *Atxn3*-10e signal in the pons in dupKI mice is of neuronal and/or astrocytic origin rather than oligodendroglial origin.

We then examined ATXN3 expression and aggregation in the brains of these mice. By Western blot, dupKi-het + N-Cre mice show increased soluble, monomeric mutant ATXN3 compared to dupKi-het littermates, recapitulating a key biochemical feature of ATXN3 in Ki mice. In contrast, dupKi-het + O-cre mice failed to show an increase in soluble ATXN3 levels (Fig. 5E). HMW ATXN3 aggregation also was markedly reduced in dupKi-het + N-Cre mice, whereas dupKi-het + O-Cre mice failed to show a reduction compared to dupKi-het mice (Fig. 5F). Finally, anti-ATXN3 immunofluorescence in the hippocampus showed dramatic loss of ATXN3 inclusions in dupKi-het + N-Cre mice, but not in dupKi-het + O-Cre mice, compared to dupKi-het littermates (Fig. 5G). Together, these findings demonstrate that correction of the exon 10 duplication selectively in oligodendrocytes does not appreciably rescue *Atxn3* mis-splicing or ATXN3 aggregation in the dupKi mouse brain. Clearly, the vast majority of mis-spliced and aggregate-prone ATXN3 in dupKi mouse brain is generated in neurons and perhaps other cell types, but not oligodendrocytes.

Finally, this selective Cre-mediated correction of exon 10 duplication either throughout the brain or only in oligodendrocytes allowed us to test whether the transcriptional changes in SCA3 mice are intrinsic to oligodendrocytes (cell-autonomous) or reflect broader changes in the brain (partially non-cell-autonomous). In dupKi mice versus dupKi mice crossed to mice expressing Nestin-

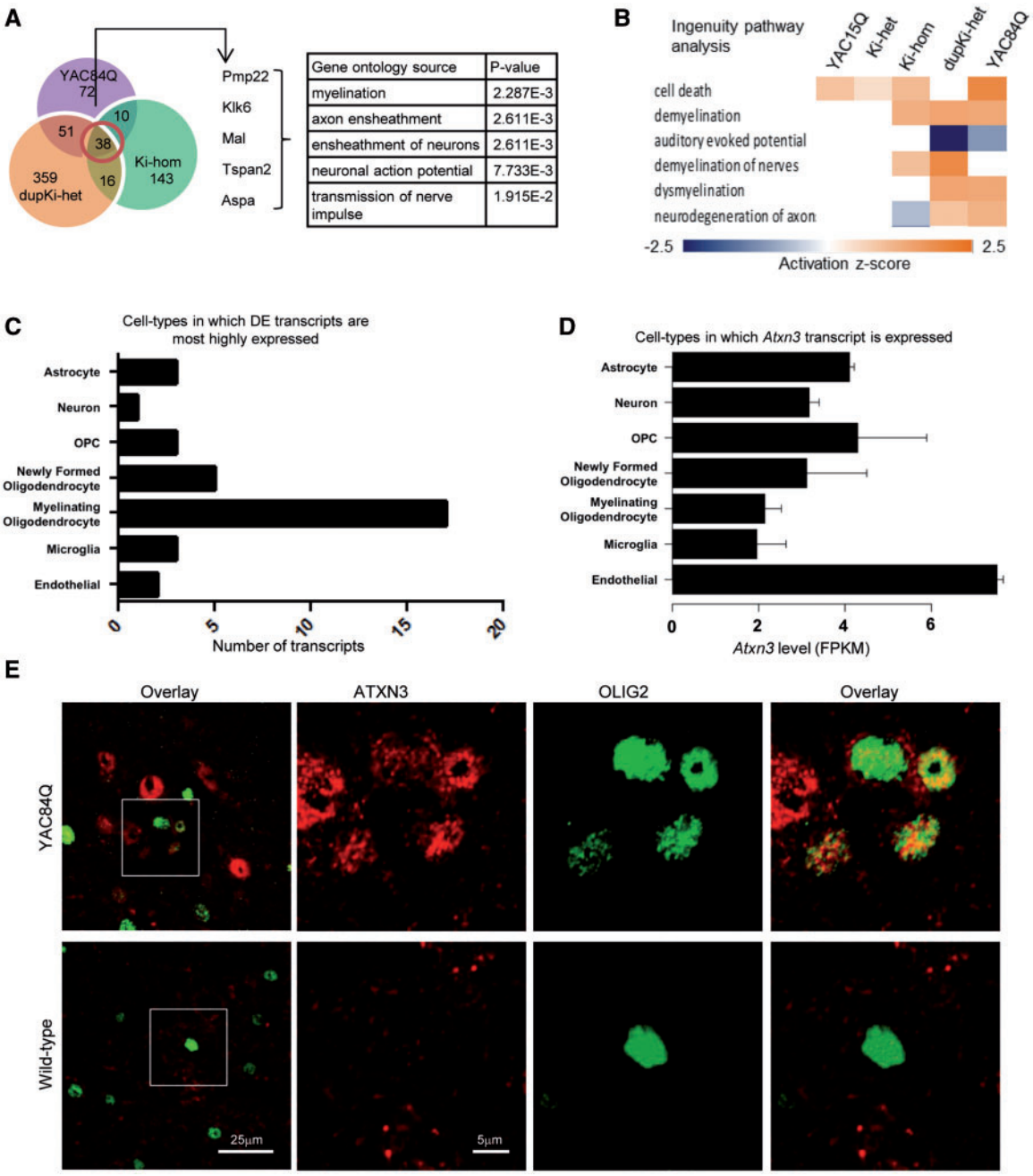

Figure 4. Bioinformatic analysis of the DE transcripts identifies robust oligodendrocyte alterations associated with mutant ATXN3 aggregation. (**A**) Gene-set enrichment analysis of the 38 shared DE transcripts between YAC84Q, Ki-hom, and dupKi-het mice revealed 5 genes significantly enriched in five 'Biological Process' categories associated with myelination. (**B**) for each genotype, visualization of the activation z-scores for the top altered Diseases and Functions categories through Ingenuity® Pathway Analysis software. This analysis highlighted several categories pointing to demyelination in mouse lines exhibiting increased aggregation. (**C**) 34 of the 38 DE transcripts commonly altered across all three aggregation-prone lines could be binned, based on the Brain RNA-Seq website (http://web.stanford.edu/group/barres_lab/brain_rnaseq.html)(26), according to the cell-type in which each is maximally expressed. The majority of these transcripts are most highly expressed in oligodendrocytes. (**D**) Brain RNA-Seq showed that *Atxn3* is widely expressed throughout the brain, including in oligodendrocytes. (**E**) Co-immunofluorescence for ATXN3 and OLIG2 in the brainstem of homozygous YAC84Q mice confirmed that ATXN3 signal is present in oligodendrocyte nuclei and is increased in comparison to wild-type oligodendrocytes. Right three images represent region within white box of leftmost image.

Cre or Olig2-Cre, we assessed transcript levels of two transcripts, *Acy3* and *Tnfrsc13c*, that are altered in SCA3 and are highly expressed in oligodendrocytes (26). RNA-seq data showed that *Acy3* and *Tnfrsf13c* are elevated in YAC84Q, dupKi-het, and Ki-hom mice, but not in Ki-het or YAC15Q mice, indicating that these oligodendrocyte-enriched transcripts may be rescued by reduced levels of mutant ATXN3 aggregation (Supplementary Material, Fig. S5). qRT-PCR confirmed marked upregulation of these two transcripts in dupKi-het mice, and this upregulation was, as expected, fully rescued in dupKi-het + N-cre mice (Fig. 5H). Remarkably, in dupKi-het + O-Cre mice, despite persistent *Atxn3* mis-splicing and ATXN3 aggregation, we observed similar rescue of these upregulated transcripts toward levels seen in wild-type and dupKi-het + N-Cre mice (Fig. 5H). Thus, the alterations in *Acy3*

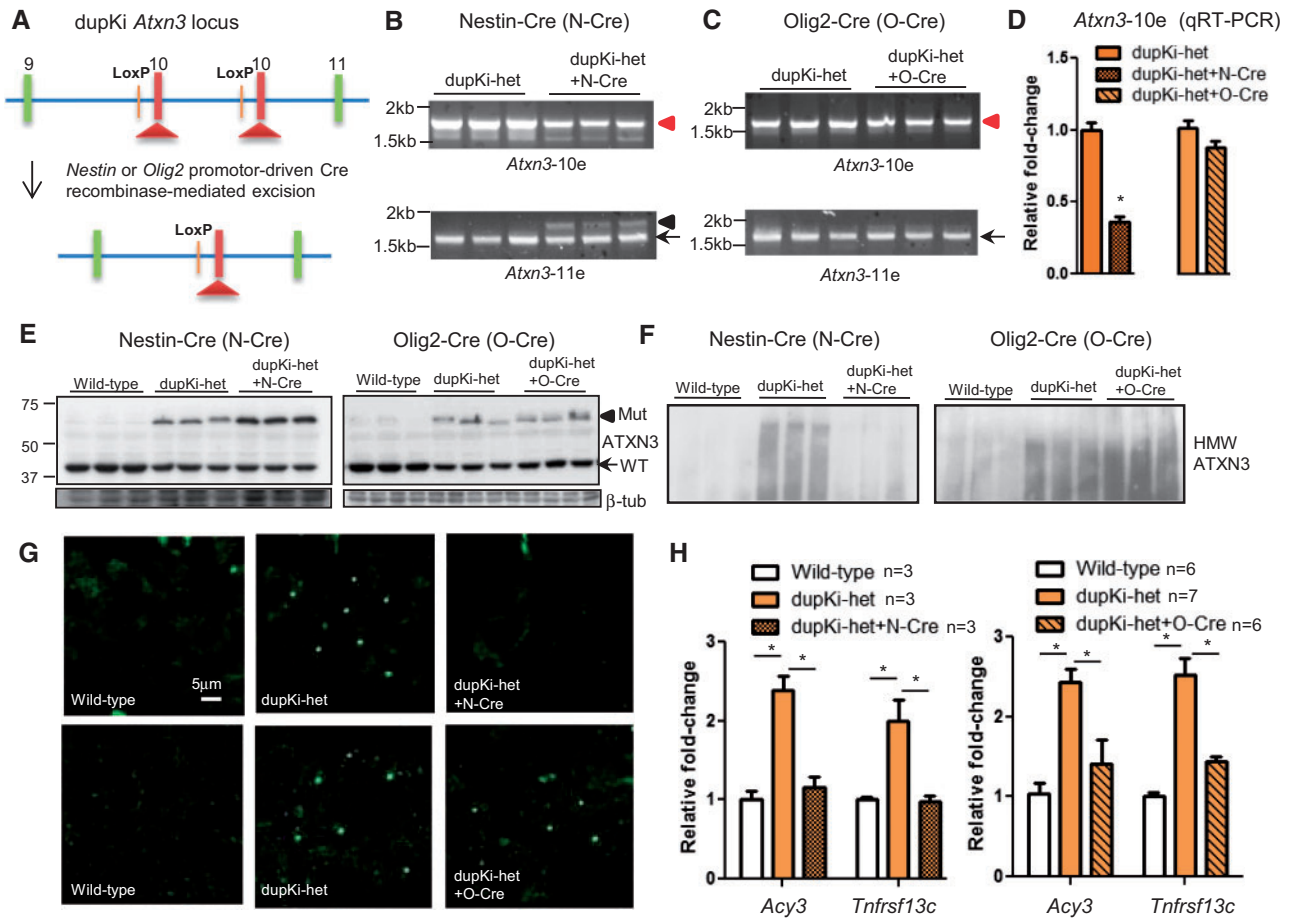

Figure 5. Oligodendrocyte-specific manipulation of the CAG repeat expansion in mice suggests mutant ATXN3 acts cell-autonomously to elicit transcriptional changes in oligodendrocytes. **(A)** The dupKi mutant *Atxn3* locus harbors two LoxP sites that allowed us to excise the duplicate exon 10 by crossing dupKi mice with mice expressing Cre under either a Nestin promoter (dupKi-het + N-Cre) to delete the duplication throughout the brain, or an Olig2 promotor (dupKi-het + O-Cre) to delete the duplication only in oligodendrocytes. **(B,C)**, RT-PCR of *Atxn3* transcripts in the brain showed that dupKi-het + N-Cre mice exhibit corrected splicing of *Atxn3*, with increased mutant *Atxn3-11e* expression (black arrowhead) and reduced *Atxn3-10e* expression (red arrowhead), whereas *Atxn3* mis-splicing was not rescued in dupKi-het + O-Cre mice. Wild-type *Atxn3-11e* (black arrow) is identified in all mice. **(D)** qRT-PCR verified that the *Atxn3*-10e transcript is significantly reduced in dupKi-het + N-Cre mice, but not in dupKi-het + O-Cre mice. **(E,F)** dupKi-het + N-Cre mice demonstrate increased soluble mutant ATXN3 (E) and markedly reduced ATXN3 aggregation in the brain (F) relative to dupKi-het mice, whereas dupKi-het + O-Cre mice show no differences in monomeric mutant ATXN3 level or HMW ATXN3 aggregation compared to dupKi-het littermates. Arrow: wild-type (WT) ATXN3, arrowhead: mutant (mut) ATXN3. **(G)**, Anti-ATXN3 immunofluorescence showed that ATXN3 inclusions in the hippocampal pyramidal layer of dupKi-het mice are no longer present in dupKi-het + N-Cre mice, whereas dupKI-het + O-Cre mice continue to exhibit inclusions similar to dupKi-het littermates. **(H)** qRT-PCR on the pons showed that the robust elevation of *Acy3* and *Tnfrsf13c* transcript levels in dupKi-het mice is rescued in both dupKi-het + N-Cre and dupKi-het + O-Cre mice. $^*P < 0.05$ by *t*-test or one-way ANOVA.

and *Tnfrsf13c*, and presumably other oligodendrocyte-associated transcripts, reflect cell-autonomous effects of aggregation-prone ATXN3 in oligodendrocytes.

Discussion

The current study, the first to evaluate a series of SCA3 mouse models differing in ATXN3 expression and aggregation, strongly supports the view that primary gain-of-function processes predominate in SCA3. This concept has been debated for SCA3, given ATXN3's known role as a deubiquitinating enzyme implicated in protein quality control (27,28). Conflicting reports on the possible protective effects of wild-type ATXN3 in animal models of SCA3 have also raised concerns that therapeutic knockdown of ATXN3 might be detrimental (9–12). Our transcriptional data, together with the observation that ATXN3-KO mice appear phenotypically normal, support the view that the repeat expansion in SCA3 does not disrupt ATXN3 function sufficiently to impact disease pathogenesis. Nevertheless, some CNS transcripts are differentially expressed in mice lacking *Atxn3*, a small number of which are also differentially expressed in SCA3 mouse models. Ongoing studies of these shared transcripts could provide additional information on ATXN3's normal role in the nervous system and its dysfunction when expanded.

Our identification of early, cell-autonomous transcriptional changes in oligodendrocytes has implications for the pathogenesis of SCA3 and perhaps other polyglutamine diseases. Neuropathological and magnetic resonance imaging studies of SCA3 and other polyglutamine diseases have frequently demonstrated significant white matter loss in the brainstem and cerebellum. White matter is also potentially disrupted in mouse models of polyglutamine disease. For example, a Q250 knock-in mouse model of Huntington disease exhibits early myelination defects, potentially precipitated by altered oligodendrocyte differentiation (29), and among SCA3 models, aged YAC84Q mice show reduced demyelination of the sciatic nerve (15). White

matter changes have largely been suspected to be secondary to neuronal loss but our study suggests, alternatively, that expression of mutant ATXN3 in oligodendrocytes directly disrupts white matter. Oligodendrocyte dysfunction could impede the propagation of neuronal action potentials, as occurs in canonical demyelinating diseases. Given the increasingly recognized role for glia in neuronal support, glial dysfunction may in turn promote neuronal dysfunction and degeneration, as demonstrated in mouse models of SCA7 (30,31) and amyotrophic lateral sclerosis (32–34).

The process by which mutant ATXN3 expression drives transcriptional changes in oligodendrocytes and the pathogenic consequences of this cell-specific transcriptional dysregulation remain key questions. Our study supports the view that the aggregation propensity of ATXN3 contributes to pathogenesis although we cannot exclude RNA-associated toxicity at this time (35,36). While cytoplasmic ATXN3 aggregates have been detected in Schwann cells of SCA3 disease tissue (37), ATXN3 aggregation in oligodendrocytes of SCA3 patient brains has not yet been demonstrated. Our preliminary examination of oligodendrocyte pathology and white matter changes in ~1-year-old dupKi-het and Ki-hom mice for did not reveal overt qualitative changes (not shown). Careful examination of SCA3 patient brains for oligodendrocyte aggregates and pathology remains a priority. Nonetheless, the expression of an expanded polyglutamine disease protein in oligodendrocytes likely has deleterious consequences. Huang and colleagues have shown that overexpressing mutant huntingtin specifically in oligodendrocytes is sufficient to drive demyelination and behavioral abnormalities in mice (38). They further implicated mutant huntingtin's binding to myelin regulatory factor as a possible mechanism eliciting such changes. SCA3 and other polyglutamine diseases may undergo similar pathogenic processes. As a next step, employing a mouse model that selectively expresses ATXN3 in specific cell types would help delineate the pathogenic effects of mutant ATXN3 in neurons versus glia. Moreover, higher powered transcriptomic studies may point to specific networks perturbed by mutant ATXN3 expression and aggregation that lead to regional degeneration.

Interpreting the causes and consequences of transcriptional changes in the brain remains challenging. At a minimum, our studies suggest specific biomarkers with which to follow disease progression. From our data ACY3 and choline dehydrogenase (CHDH) stand out, as they are known to be robustly upregulated in studies of HD mouse models (22,39,40). Interestingly, ACY3 and CHDH enzymatically break down N-acetyl aspartate (NAA) and choline, respectively, which are commonly used magnetic resonance imaging markers that are decreased in HD and a number of SCAs (41–43). The upregulation of these genes in oligodendrocytes (44) could contribute to an early decrease in these commonly used neuroimaging markers in SCA3 and perhaps other polyglutamine diseases. If so, NAA and choline would represent useful imaging biomarkers, perhaps even in pre-manifest carriers of the SCA3 mutation before substantial neuronal loss has occurred, to assess the efficacy of disease-modifying therapies.

Given our finding that the CAG repeat expansion in Ki mice does not appear to accelerate *Atxn3* mis-splicing, the extent to which CAG repeat expansions alter disease gene splicing with pathogenic consequences remains unsettled. Our prior study using the dupKi mice suggested that the repeat expansion accelerates mis-splicing of the *Atxn3* transcript (16), supporting an earlier study of HD knock-in mice in which similar altered splicing was induced by mutant *Htt* exon 1 (19). Here, however, in the corrected Ki line, we do not see accelerated *Atxn3* mis-splicing, leading us to conclude that the mis-splicing in dupKi mice likely stems, at least partly, from the presence of a PGK-TK element between the two exon 10s. It is important to note that *ATXN3*-10e and *ATXN3*-11e are both generated in human tissue and *ATXN3*-10e levels are elevated in YAC84Q mice in comparison to YAC15Q mice. Thus, mis-splicing of exon 10 to exon 11 does occur naturally. While our corrected Ki mouse suggests that the repeat expansion is not sufficient to drive Atxn3 mis-splicing, it is possible that the ~82 trinucleotide repeat is insufficient to drive mis-splicing in the context of the mouse *Atxn3* gene. Expanding the repeat to higher ranges may be required to elicit this phenomenon in mice. Nonetheless, the production of the ATXN3-10e isoform in humans may still contribute to accelerated disease protein aggregation and remains an important question to address. Consistent with this, the YAC84Q mice demonstrate far more ATXN3 aggregation than the Ki-hom mice, despite harboring the same number of mutant ATXN3-encoding genes with similar repeat lengths.

Knock-in mouse models of polyglutamine disease continue to provide valuable information on early molecular changes in disease, but typically do not exhibit behavioral phenotypes or progressive neurodegeneration. When behavioral phenotypes are present, they are generally modest and might only be precipitated by hyper-expanded repeat lengths beyond the known human disease range or so long as to cause an atypical infantile onset disease in humans (45–48). The basis for a lack of a robust phenotype in knock-in mice is likely multifactorial. First, the relatively low physiological expression of the mutant gene delays onset of deficits in comparison to overexpression models. Second, the pathophysiological processes that occur over decades in humans with a disease mutation may not be recaptured during the life span of mice. Third, the higher complexity of the human nervous system may render it more susceptible to injury and allow faster or earlier detection of neurological deficits when such intricate circuitry is disrupted. On the one hand, a disease mouse model exhibiting a robust phenotype is critical for testing possible therapeutic efficacy and understanding pathogenic cascades. On the other hand, dependence on mutant gene overexpression to obtain such phenotypes may lead to poor predictive capacity given the artificial nature of the models. Thus, knock-in mouse models provide greater value for investigations of early *in vivo* molecular changes associated with a disease mutation that cannot easily be tested in humans, as is the case in our study. Ultimately, we believe that the complementary use of multiple mouse models provides more comprehensive information than any single model alone.

Mounting studies propose a significant role for non-neuronal cells in the pathogenesis of neurodegenerative disease (49,50). An implication is that therapies targeting the disease gene may have to engage numerous cell types of the nervous system, not simply neurons. This recognition endorses a continued use of mouse models to better understand the cellular complexity of neurodegenerative diseases. It also underscores the use of mouse models employing a native gene promotor, which allows more precise exploration of the effects of the disease gene in relevant cell-types. Despite the generally modest phenotypes demonstrated by knock-in mouse models of polyglutamine disease, they remain valuable in exploring early molecular events in disease and testing disease gene-specific strategies.

Materials and Methods

Animals and ethical use

The generation of the SCA3 knock-in mice (16), YAC84Q and YAC15Q mice, (15) and ATXN3-KO mice (24) are described

previously. dupKi mice are currently available in Jackson Laboratories (B6(Cg)-Atxn3tm1Hlp/J). Deletion of the duplicate targeting vector in dupKi mice was achieved by crossing dupKi-het mice with FLPe-expressing mice (Jackson Laboratories, strain B6.Cg-g(ACTFLPe)9205Dym/J). Tissue-specific deletion of the targeting vector in the nervous system or selectively in oligodendrocytes was achieved by crossing dupKi-hom mice with Nestin-Cre mice (Jackson Laboratories, strain B6.Cg-Tg(Nes-cre)1Kln/J) or Olig2-Cre mice (51) respectively. All mice were maintained by veterinarians and animal care staff from the University of Michigan Unit for Laboratory Animal Medicine (ULAM). All manipulations and handling were performed in accordance with the guidelines of the University of Michigan Committee on Use and Care of Animals.

Immunohistochemistry and immunofluorescence

Mice were perfused with PBS, one hemisphere of the brain was fixed in 4% paraformaldehyde at 4°C for 48 h and the other hemisphere was frozen on dry ice and stored in -80°C for biochemical experiments. Fixed brains were transferred to 30% sucrose in 0.1M phosphate buffer for at least 48 h at 4°C. Brains were then serially sectioned and stained as previously described (52). Antibodies were used to stain for ATXN3 (1H9 MAB5360, Millipore, 1:1000) and OLIG2 (AB9610, Millipore, 1:500). Confocal images were acquired on Nikon-A1 (Melville, NY).

Western blotting

Tissue lysates were prepared as previously described (52) with minor modifications. Human disease brainstem tissue was kindly provided by the University of Michigan Brain Bank. Briefly, frozen tissue was homogenized in 10 vol RIPA + protease inhibitor (PI) cocktail containing RIPA buffer (50 mM Tris–HCl pH 7.4, 150 mM sodium chloride, 0.1% SDS, 0.5% sodium deoxycholate, 1% NP-40) and protease inhibitors (Complete Mini tablets, Roche). Homogenates were centrifuged at 1500*g* for 15 min at 4 °C, and supernatants (soluble fraction) were transferred to a new tube and assayed for protein concentration using bicinchoninic acid (BCA) (Pierce). The soluble fractions were diluted to a final concentration of 4 μg/μl in RIPA + PI + 6x loading buffer (with the 6x concentration being 0.35 M Tris-HCl, 10% SDS, 36% glycerol, 0.6 M dithiothreitol, and 12% bromophenol blue), and boiled for 5 min. Samples were then separated by SDS-PAGE, transferred to polyvinylidene fluoride (PVDF) membrane, and blotted. Antibodies include rabbit polyclonal anti-MJD 1:10,000 (53), rabbit polyclonal anti-ACY3 16786-1-AP 1:2000 (Proteintech), rabbit polyclonal anti-BAFF receptor antibody ab5965 1:300 (Abcam), and rabbit polyclonal β-tubulin #2145S 1:5000 (Cell Signaling).

To detect high molecular weight ATXN3 aggregates, a mouse brain hemisphere was homogenized in 1 ml RIPA + PI, sonicated briefly, incubated on ice for 30 min, and centrifuged at 12,000*g* for 20 min at 4 °C. The supernatant was saved and assayed for protein concentration. 1 mg of protein was then incubated overnight at 4 °C in 1 μl of MJD antibody + 20 μl EZview™ Red Protein A Affinity Gel (Sigma Aldrich) previously washed 3x with RIPA. The gel was then pelleted, washed 3 x 10 min with RIPA bufer, and eluted by boiling for 5 min in 20 ul 2x loading buffer. The lysate was resolved on a 3-8% Tris-acetate gel, transferred to PVDF, and blotted with anti-MJD antibody as above.

Motor behavior

Motor function was assessed on SCA3 knock-in mice as previously reported (54), including tests on accelerating rotarod (4–40 rpm in 5 min), balance beam (5 mm square), and locomotor activity in an open field chamber for 30 min. Wild-type, Ki-het, and dupKi-het mice ranging from 55 to 61 weeks of age were tested. All mice underwent three days of training on balance beam and accelerating rotarod. We analyzed balance beam and rotarod data for the fourth day of testing, along with locomotor behavior, using a Student's *t*-test with a Bonferroni post-hoc correction. Graphing and statistics were performed on Prism® software (San Diego, CA, USA).

RNA extraction, RNA sequencing, and gene expression analysis

RNA was chloroform extracted from pons using TRIzol® (Life Technologies) and purified using the RNeasy kit with on-column DNase I digestion (Qiagen). Purified RNA was submitted to the University of Michigan Bioinformatics Core for library generation (Illumina TruSeq) sequenced on Illumina HiSeq 2000 (100×100 paired-end, 2 lanes). We used FastQC for quality control and Trimmomatic (55) for removing contamination of primers/adapters. The sequencing reads for each mouse were aligned to mm38 using TopHat2 (56). The number of differential expressed (DE) transcripts were identified through DESeq were defined by the following threshold: DESeq.padj 0.1 cutoff, fold-change < 0.8 and > 1.2. For the 171 DE transcripts identified for YAC84Q mice, we generated normalized FPKM values through CuffDiff and calculated fold-change relative to wild-type for 163 of the 171 transcripts. These values were inputted into MultiExperiment Viewer (http://www.tm4.org/mev.html) to generate a heat map.

The identified DE transcripts were further analyzed using different software. Gene enrichment analysis was done in ToppFun under the ToppGene suite (https://toppgene.cchmc.org/enrichment.jsp) (25). In addition, the DE transcripts for five genotypes (YAC15Q, Ki-het, Ki-hom, dupKi-het, and YAC84Q) were entered into Ingenuity® Pathway Analysis to identify the top activation z-scores under Diseases & Functions categories. In this analysis, a positive z-score is a prediction that our input DE genes activate that pathway, whereas a negative z-score predicts that the DE genes inhibit that pathway (57). The absolute value of the z-score reflects the number of DE genes enriched in that category. Cell-type expression was determined from publically-available RNA-seq data on mouse cerebral cortex (http://web.stanford.edu/group/barres_lab/brain_rnaseq.html) (26).

Quantitative and non-quantitative RT-PCR

For RT-PCR, 1 μg of RNA was reverse-transcribed using iScript™, amplified by standard PCR, and resolved on 1% agarose. For RT-PCR of double exon-10 transcripts, 2 μg total RNA was reverse-transcribed using the 5'RACE kit (Thermo Fisher), with which we used a reverse-facing primer against a region in the 3' UTR of *Atxn3* (CACTGTAATCACACAGACAATGTTA). Quantitative RT-PCR (qRT-PCR) was performed using SYBR® Green Master Mix and run on BioRad iCycler with MyIQ single color real-time PCR detection system module with the following parameters: 95°C at 3 min, (95°C 10 s, 55°C 30 s) × 40, 95°C 1 min, 55°C 1 min. The fold-change in transcript levels was calculated using the ΔΔCt method with *Gapdh* as a control (58). The primers are listed below and were all purchased from Integrated Genomics

Primers

Amplicon	Forward primer (5' to 3')	Reverse primer (5' to 3')	Experiment
Atxn3 ex1 – int10	GACAAATAAACATGGAGTCCATCTTC	CGAGGATCTTGGGTATCGAGT	RT-PCR
Atxn3 ex1 – ex 11	GACAAATAAACATGGAGTCCATCTTC	CAAAGTGTGTGAGTAGCAAAATGACT	RT-PCR
Atxn3 ex10 (3'end) - ex10 (5'end)	GGACGTAGGAGCGACCAAG	ATATGAAAGGGGTCCAGGTCG	RT-PCR
Atxn3 exon 9 – exon 11	CTGCGGAGGAGACGAGAAG	CAAAGTGTGTGAGTAGCAAAATGACT	RT-PCR
Atxn3 exon 10- exon 11	GGACGTAGGAGCGACCAAG	CAAAGTGTGTGAGTAGCAAAATGACT	RT-PCR
Gapdh	CTTTGTCAAGCTCATTTCCTG	TCTTGCTCAGTGTCCTTG	qRT-PCR
Acy3	CTTCAACCAAGGCATGGACT	TCAAAGTCATGGTCCTGCAG	qRT-PCR
Polr2a	CAGGACACTGGACCGCTCAT	GCATAATATTCTCAGAGACTCCCTTCA	qRT-PCR
Smoc1	TTCAGGAAGAAAAGATGATGGCT	ATCCATAAGGTGGGGGCTGT	qRT-PCR
Prob1	TTCCCCGTGAGACTCCTGAT	CAACCCTACTGGGAACCACC	qRT-PCR
Tnfrsf13c	CGCTCAAAGAAGATGCAGACAG	CTGTCTTGGTGGTCACCAGCT	qRT-PCR
Slc45a3	GGCCCGGAGACACTATGAT	TCCATGACCAGGGAGAAGAC	qRT-PCR
Tmprss5	GGAGTGAGCCGTGAGGAAG	GATCCTCTCCATTTATTCTGAAAGA	qRT-PCR
Mobp	GAGGAGGACTGGATCTGCTG	TCACTTCTTCCTTGGGGTTG	qRT-PCR
Qdpr	CTGGCAGGGAGAACAGTG	ATCGGGGTATCCAGGGTAA	qRT-PCR
Glul	GTTTGGAATGGAGCAGGAATA	GCTCCCACACCGCAGTAA	qRT-PCR
Il33	AGGGAGAAATCACGGCAGAA	TATTTTGCAAGGCGGGACCA	qRT-PCR

Technologies. Graphing and statistics were performed on Prism ® software.

Supplementary Material

Supplementary Material is available at *HMG* online.

Acknowledgements

We thank members of the Paulson lab for helpful discussion on the manuscript. We thank Dr. Hayley McLaughlin and Ms. Svetlana Fischer for providing tissue samples for immunofluorescent staining. We thank Drs. Chun-Chi Liang, Dhananjay Yellajoshyula, and William Dauer for discussion and help with utilizing Nestin-Cre and Olig2-Cre mice. Finally, we thank the reviewers for their helpful suggestions and feedback. This work utilized core services provided by the University of Michigan DNA sequencing core.

Conflict of Interest statement. None declared.

Funding

National Institutes of Health [RO1NS038712 to H.L.P.; F31NS083167 to B.R.].

References

1. Rüb, U., Schöls, L., Paulson, H., Auburger, G., Kermer, P., Jen, J.C., Seidel, K., Korf, H.-W. and Deller, T. (2013) Clinical features, neurogenetics and neuropathology of the polyglutamine spinocerebellar ataxias type 1, 2, 3, 6 and 7. *Prog. Neurobiol.*, **104**, 38–66.
2. Adegbuyiro, A., Sedighi, F., Pilkington, A.W., Groover, S. and Legleiter, J. (2017) Proteins containing expanded polyglutamine tracts and neurodegenerative disease. *Biochemistry*, **56**, 1199–1217.
3. Arrasate, M., Mitra, S., Schweitzer, E.S., Segal, M.R. and Finkbeiner, S. (2004) Inclusion body formation reduces levels of mutant huntingtin and the risk of neuronal death. *Nature*, **431**, 805–810.
4. Saudou, F., Finkbeiner, S., Devys, D. and Greenberg, M.E. (1998) Huntingtin acts in the nucleus to induce apoptosis but death does not correlate with the formation of intranuclear inclusions. *Cell*, **95**, 55–66.
5. Kurosawa, M., Matsumoto, G., Kino, Y., Okuno, M., Kurosawa-Yamada, M., Washizu, C., Taniguchi, H., Nakaso, K., Yanagawa, T., Warabi, E. *et al.* (2014) Depletion of p62 reduces nuclear inclusions and paradoxically ameliorates disease phenotypes in Huntington's model mice. *Hum. Mol. Genet.*, **24**, 1092–1105.
6. Sweeney, P., Park, H., Baumann, M., Dunlop, J., Frydman, J., Kopito, R., McCampbell, A., Leblanc, G., Venkateswaran, A., Nurmi, A. *et al.* (2017) Protein misfolding in neurodegenerative diseases: implications and strategies. *Transl. Neurodegener.*, **6**, 6
7. Yerbury, J.J., Ooi, L., Dillin, A., Saunders, D.N., Hatters, D.M., Beart, P.M., Cashman, N.R., Wilson, M.R. and Ecroyd, H. (2016) Walking the tightrope: Proteostasis and neurodegenerative disease. *J. Neurochem.*, **137**, 489–505.
8. Hipp, M.S., Park, S.H. and Hartl, U.U. (2014) Proteostasis impairment in protein-misfolding and -aggregation diseases. *Trends Cell Biol.*, **24**, 506–514.
9. Warrick, J.M., Morabito, L.M., Bilen, J., Gordesky-Gold, B., Faust, L.Z., Paulson, H.L. and Bonini, N.M. (2005) Ataxin-3 suppresses polyglutamine neurodegeneration in Drosophila by a ubiquitin-associated mechanism. *Mol. Cell*, **18**, 37–48.
10. Schmitt, I., Linden, M., Khazneh, H., Evert, B.O., Breuer, P., Klockgether, T. and Wuellner, U. (2007) Inactivation of the mouse Atxn3 (ataxin-3) gene increases protein ubiquitination. *Biochem. Biophys. Res. Commun.*, **362**, 734–739.
11. Alves, S., Nascimento-Ferreira, I., Dufour, N., Hassig, R., Auregan, G., Nóbrega, C., Brouillet, E., Hantraye, P., Pedroso de Lima, M.C., Déglon, N. *et al.* (2010) Silencing ataxin-3 mitigates degeneration in a rat model of Machado-Joseph disease: no role for wild-type ataxin-3?. *Hum. Mol. Genet.*, **19**, 2380–2394.
12. Hübener, J. and Riess, O. (2010) Polyglutamine-induced neurodegeneration in SCA3 is not mitigated by non-expanded

ataxin-3: conclusions from double-transgenic mouse models. *Neurobiol. Dis.*, **38**, 116–124.
13. Kretzschmar, D., Tschäpe, J., Da Cruz, A.B., Asan, E., Poeck, B., Strauss, R. and Pflugfelder, G.O. (2005) Glial and neuronal expression of polyglutamine proteins induce behavioral changes and aggregate formation in Drosophila. *Glia*, **49**, 59–72.
14. Colomer Gould, V.F. (2012) Mouse models of spinocerebellar ataxia type 3 (Machado-Joseph disease). *Neurotherapeutics*, **9**, 285–296.
15. Cemal, C.K., Carroll, C.J., Lawrence, L., Lowrie, M.B., Ruddle, P., Al-Mahdawi, S., King, R.H.M., Pook, M. a., Huxley, C. and Chamberlain, S. (2002) YAC transgenic mice carrying pathological alleles of the MJD1 locus exhibit a mild and slowly progressive cerebellar deficit. *Hum. Mol. Genet.*, **11**, 1075–1094.
16. Ramani, B., Harris, G.M., Huang, R., Seki, T., Murphy, G.G., Costa, M.D.C., Fischer, S., Saunders, T.L., Xia, G., McEachin, R.C. *et al.* (2015) A knockin mouse model of spinocerebellar ataxia type 3 exhibits prominent aggregate pathology and aberrant splicing of the disease gene transcript. *Hum. Mol. Genet.*, **24**, 1211–1224.
17. Switonski, P.M., Szlachcic, W.J., Krzyzosiak, W.J. and Figiel, M. (2015) A new humanized ataxin-3 knock-in mouse model combines the genetic features, pathogenesis of neurons and glia and late disease onset of SCA3/MJD. *Neurobiol. Dis.*, **73**, 174–188.
18. Harris, G.M., Dodelzon, K., Gong, L., Gonzalez-Alegre, P. and Paulson, H.L. (2010) Splice isoforms of the polyglutamine disease protein ataxin-3 exhibit similar enzymatic yet different aggregation properties. *PLoS One*, **5**, e13695.
19. Sathasivam, K., Neueder, A., Gipson, T.A., Landles, C., Benjamin, A.C., Housman, D.E. and Bates, G.P. (2013) Aberrant splicing of HTT generates the pathogenic exon 1 protein in Huntington disease. *Proc. Natl. Acad. Sci. U. S. A*, **110**, 2366–2370.
20. Mohan, R.D., Abmayr, S.M. and Workman, J.L. (2014) The expanding role for chromatin and transcription in polyglutamine disease. *Curr. Opin. Genet. Dev.*, **26**, 96–104.
21. Kumar, A., Vaish, M. and Ratan, R.R. (2014) Transcriptional dysregulation in Huntington's disease: a failure of adaptive transcriptional homeostasis. *Drug Discov. Today*, **19**, 956–962.
22. Langfelder, P., Cantle, J.P., Chatzopoulou, D., Wang, N., Gao, F., Al-Ramahi, I., Lu, X.-H., Ramos, E.M., El-Zein, K., Zhao, Y. *et al.* (2016) Integrated genomics and proteomics define huntingtin CAG length–dependent networks in mice. *Nat. Neurosci.*, **19**, 623–633.
23. Valor, L.M., Guiretti, D., Lopez-Atalaya, J.P. and Barco, A. (2013) Genomic landscape of transcriptional and epigenetic dysregulation in early onset polyglutamine disease. *J. Neurosci.*, **33**, 10471–10482.
24. Reina, C.P., Nabet, B.Y., Young, P.D. and Pittman, R.N. (2012) Basal and stress-induced Hsp70 are modulated by ataxin-3. *Cell Stress Chaperones*, **17**, 729–742.
25. Chen, J., Bardes, E.E., Aronow, B.J. and Jegga, A.G. (2009) ToppGene Suite for gene list enrichment analysis and candidate gene prioritization. *Nucleic Acids Res.*, **37**, 305–311.
26. Zhang, Y., Chen, K., Sloan, S. a., Bennett, M.L., Scholze, A.R., Keeffe, S.O., Phatnani, H.P., Guarnieri, X.P., Caneda, C., Ruderisch, N. *et al.* (2014) An RNA-sequencing transcriptome and splicing database of glia, neurons, and vascular cells of the cerebral cortex. *J. Neurosci.*, **34**, 11929–11947.
27. Burnett, B., Li, F. and Pittman, R.N. (2003) The polyglutamine neurodegenerative protein ataxin-3 binds polyubiquitylated proteins and has ubiquitin protease activity. *Hum. Mol. Genet.*, **12**, 3195–3205.
28. Mao, Y., Senic-Matuglia, F., Di Fiore, P.P., Polo, S., Hodsdon, M.E. and De Camilli, P. (2005) Deubiquitinating function of ataxin-3: insights from the solution structure of the Josephin domain. *Proc. Natl. Acad. Sci. U. S. A*, **102**, 12700–12705.
29. Jin, J., Peng, Q., Hou, Z., Jiang, M., Wang, X., Langseth, a. J., Tao, M., Barker, P.B., Mori, S., Bergles, D.E. *et al.* (2015) Early white matter abnormalities, progressive brain pathology and motor deficits in a novel knock-in mouse model of Huntington's disease. *Hum. Mol. Genet.*, **24**, 2508–2527.
30. Custer, S.K., Garden, G. a., Gill, N., Rueb, U., Libby, R.T., Schultz, C., Guyenet, S.J., Deller, T., Westrum, L.E., Sopher, B.L. *et al.* (2006) Bergmann glia expression of polyglutamine-expanded ataxin-7 produces neurodegeneration by impairing glutamate transport. *Nat. Neurosci.*, **9**, 1302–1311.
31. Furrer, S.A., Mohanachandran, M.S., Waldherr, S.M., Chang, C., Damian, V.A., Sopher, B.L., Garden, G.A. and La Spada, A.R. (2011) Spinocerebellar ataxia type 7 cerebellar disease requires the coordinated action of mutant ataxin-7 in neurons and glia, and displays non-cell-autonomous bergmann glia degeneration. *J. Neurosci.*, **31**, 16269–16278.
32. Sambataro, F. and Pennuto, M. (2012) Cell-autonomous and non-cell-autonomous toxicity in polyglutamine diseases. *Prog. Neurobiol.*, **97**, 152–172.
33. Nonneman, A., Robberecht, W. and Den Bosch, L.V. (2014) The role of oligodendroglial dysfunction in amyotrophic lateral sclerosis. *Neurodegener. Dis. Manag.*, **4**, 223–239.
34. Philips, T., Bento-Abreu, A., Nonneman, A., Haeck, W., Staats, K., Geelen, V., Hersmus, N., Küsters, B., Van Den Bosch, L., Van Damme, P. *et al.* (2013) Oligodendrocyte dysfunction in the pathogenesis of amyotrophic lateral sclerosis. *Brain*, **136**, 471–482.
35. Nalavade, R., Griesche, N., Ryan, D.P., Hildebrand, S. and Krauss, S. (2013) Mechanisms of RNA-induced toxicity in CAG repeat disorders. *Cell Death Dis.*, **4**, 1–11.
36. Rue, L., Banez-Corone, M., Creus-Muncunill, J., Giralt, A., Alcala-Vida, R., Mentxaka, G., Kagerbauer, B., Zomeno-Abellan, M.T., Aranda, Z., Venturi, V. *et al.* (2016) Targeting CAG repeat RNAs reduces Huntington's disease phenotype independently of huntingtin levels. *J. Clin. Invest.*, **126**, 4319–4330.
37. Suga, N., Katsuno, M., Koike, H., Banno, H., Suzuki, K., Hashizume, A., Mano, T., Iijima, M., Kawagashira, Y., Hirayama, M. *et al.* (2014) Schwann cell involvement in the peripheral neuropathy of spinocerebellar ataxia type 3. *Neuropathol. Appl. Neurobiol.*, **40**, 628–639.
38. Huang, B., Wei, W., Wang, G., Gaertig, M.A., Feng, Y., Wang, W., Li, X.-J. and Li, S. (2015) Mutant Huntingtin downregulates myelin regulatory factor-mediated myelin gene expression and affects mature oligodendrocytes. *Neuron*, **85**, 1212–1226.
39. Becanovic, K., Pouladi, M. a., Lim, R.S., Kuhn, A., Pavlidis, P., Luthi-Carter, R., Hayden, M.R. and Leavitt, B.R. (2010) Transcriptional changes in Huntington disease identified using genome-wide expression profiling and cross-platform analysis. *Hum. Mol. Genet.*, **19**, 1438–1452.
40. Giles, P., Elliston, L., Higgs, G.V., Brooks, S.P., Dunnett, S.B. and Jones, L. (2012) Longitudinal analysis of gene expression and behaviour in the HdhQ150 mouse model of Huntington's disease. *Brain Res. Bull.*, **88**, 199–209.
41. Lopes, T.M., D'Abreu, A., França, M.C., Yasuda, C.L., Betting, L.E., Samara, A.B., Castellano, G., Somazz, J.C., Balthazar,

M.L.F., Lopes-Cendes, I. *et al.* (2013) Widespread neuronal damage and cognitive dysfunction in spinocerebellar ataxia type 3. *J. Neurol.*, **260**, 2370–2379.
42. Sanchez-Pernaute, R., Garcia-Segura, J., del Barrio Alba, A., Viano, J. and de Yebenes, J. (1999) Clinical correlation of striatal 1H MRS changes in Huntington's diseaseTitle. *Neurology*, **53**, 806–812.
43. Klaes, A., Reckziegel, E., Franca, M.C., Rezende, T.J.R., Vedolin, L.M., Jardim, L.B. and Saute, J. a. (2016) MR imaging in Spinocerebellar ataxias: A systematic review. *Am. J. Neuroradiol.*, **37**, 1405–1412.
44. Nordengen, K., Heuser, C., Rinholm, J.E.G., Matalon, R. and Gundersen, V. (2015) Localisation of N-acetylaspartate in oligodendrocytes/myelin. *Brain Struct. Funct.*, **220**, 899–917.
45. Lin, C., Tallaksen-greene, S., Chien, W., Cearley, J.A., Jackson, W.S., Crouse, A.B., Ren, S., Li, X., Albin, R.L. and Detloff, P.J. (2001) Neurological abnormalities in a knock-in mouse model of Huntington's disease. *Hum. Mol. Genet.*, **10**, 137–144.
46. Bowman, A.B., Yoo, S.-Y., Dantuma, N.P. and Zoghbi, H.Y. (2005) Neuronal dysfunction in a polyglutamine disease model occurs in the absence of ubiquitin-proteasome system impairment and inversely correlates with the degree of nuclear inclusion formation. *Hum. Mol. Genet.*, **14**, 679–691.
47. Yang, S., Huang, S., Gaertig, M. a., Li, X.-J. and Li, S. (2014) Age-dependent decrease in chaperone activity impairs MANF expression, leading to Purkinje cell degeneration in inducible SCA17 mice. *Neuron*, **81**, 349–365.
48. Watase, K., Weeber, E.J., Xu, B., Antalffy, B., Yuva-Paylor, L., Hashimoto, K., Kano, M., Atkinson, R., Sun, Y., Armstrong, D.L. *et al.* (2002) A long CAG repeat in the mouse Sca1 locus replicates SCA1 features and reveals the impact of protein solubility on selective neurodegeneration. *Neuron*, **34**, 905–919.
49. Verkhratsky, A., Parpura, V., Pekna, M., Pekny, M. and Sofroniew, M. (2014) Glia in the pathogenesis of neurodegenerative diseases. *Biochem. Soc. Trans.*, **42**, 1291–1301.
50. Lobsiger, C.S. and Cleveland, D.W. (2007) Glial cells as intrinsic components of non-cell-autonomous neurodegenerative disease. *Nat. Neurosci.*, **10**, 1355–1360.
51. Schüller, U., Heine, V.M., Mao, J., Kho, A.T., Dillon, A.K., Han, Y.G., Huillard, E., Sun, T., Ligon, A.H., Qian, Y. *et al.* (2008) Acquisition of granule neuron precursor identity is a critical determinant of progenitor cell competence to form Shh-induced medulloblastoma. *Cancer Cell*, **14**, 123–134.
52. Williams, A.J., Knutson, T.M., Colomer Gould, V.F. and Paulson, H.L. (2009) In vivo suppression of polyglutamine neurotoxicity by C-terminus of Hsp70-interacting protein (CHIP) supports an aggregation model of pathogenesis. *Neurobiol. Dis.*, **33**, 342–353.
53. Paulson, H.L., Das, S.S., Crino, P.B., Perez, M.K., Patel, S.C., Gotsdiner, D., Fischbeck, K.H. and Pittman, R.N. (1997) Machado-Joseph disease gene product is a cytoplasmic protein widely expressed in brain. *Ann. Neurol.*, **41**, 453–462.
54. Heng, M.Y., Tallaksen-Greene, S.J., Detloff, P.J. and Albin, R.L. (2007) Longitudinal evaluation of the Hdh(CAG)150 knock-in murine model of Huntington's disease. *J. Neurosci.*, **27**, 8989–8998.
55. Bolger, A.M., Lohse, M. and Usadel, B. (2014) Trimmomatic: A flexible trimmer for Illumina sequence data. *Bioinformatics*, **30**, 2114–2120.
56. Kim, D., Pertea, G., Trapnell, C., Pimentel, H., Kelley, R. and Salzberg, S.L. (2013) TopHat2: accurate alignment of transcriptomes in the presence of insertions, deletions and gene fusions. *Genome Biol.*, **14**, 1–13.
57. Kramer, A., Green, J., Pollard, J. and Tugendreich, S. (2014) Causal analysis approaches in ingenuity pathway analysis. *Bioinformatics*, **30**, 523–530.
58. Livak, K.J. and Schmittgen, T.D. (2001) Analysis of relative gene expression data using real-time quantitative PCR and the 2(-Delta Delta C(T)) Method. *Methods*, **25**, 402–408.